Phase-field modeling of cyclic phase transformations in low-carbon steels

Article *in* Computational Materials Science · February 2015

DOI: 10.1016/j.commatsci.2015.01.023

3 authors, including:

Benqiang Zhu
University of British Columbia - Vancouver
7 PUBLICATIONS **25** CITATIONS

SEE PROFILE

Hao Chen
Tsinghua University
37 PUBLICATIONS **317** CITATIONS

SEE PROFILE

Computational Materials Science 108 (2015) 333–341

Contents lists available at ScienceDirect

Computational Materials Science

journal homepage: www.elsevier.com/locate/commatsci

Phase-field modeling of cyclic phase transformations in low-carbon steels

Benqiang Zhu *, Hao Chen, Matthias Militzer

Centre for Metallurgical Process Engineering, The University of British Columbia, Vancouver V6T1Z4, Canada

ARTICLE INFO

Article history:
Received 7 December 2014
Received in revised form 14 January 2015
Accepted 17 January 2015
Available online 10 February 2015

Keywords:
Cyclic phase transformation
Phase-field modeling
Low-carbon steels
Gibbs energy dissipation
Solute drag

ABSTRACT

A phase-field model has been developed to describe microstructure evolution during cyclic phase transformations for two low-carbon steels (Fe–0.1 wt%C, Fe–0.1 wt%C–0.5 wt%Mn). The austenite–ferrite transformations are assumed to occur under negligible-partition conditions for Mn and only long-range diffusion of carbon is considered. A Gibbs-energy dissipation model has been integrated with the phase-field model to describe the stagnant stages during cyclic phase transformations in the ternary alloy. Experimental results, e.g. the stagnant stages and the cyclic phase transformation kinetics, have been successfully replicated with 2D phase-field simulations.

1. Introduction

The mechanism of the austenite formation and decomposition in the intercritical region is of great interest due to its practical importance in steel design and production, and it has been investigated with a number of experimental approaches, e.g. conventional isothermal or continuous heating/cooling experiments [1,2] and decarburization experiments [3], and modeling techniques, e.g. one-dimensional sharp-interface models [2,4,5] and multi-dimensional mesoscale models [6–10].

Chen et al. [11,12] proposed a cyclic partial phase transformation approach, in which the complex nucleation process can be avoided, to study the austenite-to-ferrite transformation and its reverse transformation in Fe–C–Mn alloys. The approach employs a cyclic heat treatment in the intercritical region where partial austenite-to-ferrite and ferrite-to-austenite transformations take place alternatively. For cyclic partial transformations, a special feature has been observed, i.e. a particular temperature range during both heating and cooling where the change in phase fractions remains negligible. Such temperature ranges are termed "stagnant stages". In order to explain this special feature, one-dimensional sharp-interface models (Local-Equilibrium model (LE) [13–15] and Para-equilibrium model (PE) [16,17]) were used to simulate the cyclic phase transformations in the Fe–C–Mn alloys [12]. It was found that the LE model considering redistribution of substitutional elements can replicate the stagnant stages quite well, whereas the PE model predicts no stagnant stages. Thus it was concluded that the stagnant stage is due to the redistribution of substitutional alloying elements near the interface. The LE model, albeit powerful, is limited to 1D simulation so far, due to high computational cost, since fine meshes are required to resolve the diffusion length of substitutional elements.

In contrast, Gamsjäger et al. proposed a one-dimensional mixed-mode model to investigate the stagnant stages in cyclic phase transformations [18]. In the mixed-mode model, the substitutional elements were assumed to be immobile in their sublattice and effective austenite/ferrite interface mobilities were used to account for the effect of solutes on cyclic phase transformations. In order to obtain a good description of the transformation kinetics, the austenite/ferrite interface mobility was assumed to not obey an Arrhenius relationship, i.e. the activation energy of mobility was taken as a linear function of temperature. This assumption leads to a great variation of the austenite/ferrite interface mobility with temperature such that a small mobility at the stagnant stages is obtained to mimic the sluggish interface migration. Further, the fitted mobility values are different for the austenite-to-ferrite transformation and the reverse ferrite-to-austenite transformation.

The effective-mobility approach used by Gamsjäger et al. [18] has been widely employed in the past and integrated with mesoscale models, e.g. phase-field models [8,9,19]. This approach has been applied successfully in simulating the austenite-to-ferrite transformation during continuous cooling [8,19,20]. In selected

* Corresponding author at: The University of British Columbia, 309 6350 Stores Rd, Vancouver V6T1Z4, Canada. Tel.: +1 6048227886.
E-mail address: zhubenqiang@gmail.com (B. Zhu).

http://dx.doi.org/10.1016/j.commatsci.2015.01.023
0927-0256/

cases, however, the effective mobility was found to depend unreasonably on cooling rate which was attributed to potential segregation of alloying elements at migrating interfaces [21,22]. Two theories have been developed to model the effects of solute segregation on slowing down phase transformations: (i) solute drag theory [23,24]; (ii) Gibbs-energy dissipation theory [25]. In the solute drag theory, a drag pressure is assumed to be exerted on a migrating interface by segregated solute atoms. In the Gibbs-energy dissipation theory, it is proposed that solute diffusion inside a migrating interface (trans-interface diffusion) leads to dissipation of Gibbs energy [25]. Hillert found these two theories were actually equivalent, i.e. the solute drag pressure is equal to the dissipated Gibbs-energy [26]. To be consistent, the term "Gibbs-energy dissipation" will be used in the present work. Based on these two theories, several models have been developed to investigate the effects of alloying elements on phase transformation in steels. By making suitable assumptions for the solute-interface binding energy and the trans-interface diffusivity they have been successfully applied to describing the austenite-to-ferrite transformation [2,4,5,22]. In all these models, solute diffusion is assumed to occur inside the interface only but not in the bulk. These models have yet to be used to describe cyclic phase transformations.

The present paper is devoted to developing a two-dimensional phase-field model capable of accounting for microstructural morphologies and describing quantitatively the experimentally measured transformation kinetics during cyclic heat treatments of low-carbon steels. In particular, Gibbs-energy dissipation by trans-interface diffusion of solutes is taken into account in the phase-field model. The model is applied to two low-carbon steels (Fe–0.1 wt%C, Fe–0.1 wt%C–0.5 wt%Mn) and validated with experimental observations.

2. Method

2.1. Phase-field model

A single-phase-field model [27] is used in this work:

$$\frac{d\phi}{dt} = m_{\alpha\gamma}\left\{\sigma_{\alpha\gamma}\left[\nabla^2\phi + \frac{\pi^2}{\eta^2}\left(\phi - \frac{1}{2}\right)\right] + \frac{\pi}{\eta}\sqrt{\phi(1-\phi)}\Delta G_{\alpha\to\gamma}\right\} \quad (1)$$

where α denotes ferrite, γ denotes austenite, the phase-field variable ϕ represents the local fraction of austenite, η is the interface thickness, $m_{\alpha\gamma}$ is the ferrite/austenite interface mobility, $\sigma_{\alpha\gamma}$ is the interface energy and $\Delta G_{\alpha\to\gamma}$ is the driving pressure. The mobilities are assumed to obey an Arrhenius relationship, i.e.

$$m_{\alpha\gamma} = m^0_{\alpha\gamma}\exp\left(-\frac{Q_{\alpha\gamma}}{RT}\right) \quad (2)$$

where $m^0_{\alpha\gamma}$ is the pre-factor, $Q_{\alpha\gamma}$ is the activation energy, T is the temperature and R is the ideal gas constant.

The driving pressure in the phase-field model is a function of both temperature and carbon concentrations for austenite–ferrite transformations in low-carbon steels. Long-range diffusion of carbon is considered and coupled to the phase-field model. Thus, the model is of mixed-mode character [28], i.e. both long-range diffusion of carbon and interface reaction are taken into account. The carbon diffusion equation is given by:

$$\frac{\partial C}{\partial t} = \nabla(D_\alpha(1-\phi)\nabla C_\alpha + D_\gamma\phi\nabla C_\gamma) \quad (3)$$

where D_α and D_γ are the carbon diffusivities in ferrite and austenite, C is the local carbon concentration which, in the interface region, is the sum of the carbon concentrations (C_α and C_γ) in both phases weighted with the phase-field parameter:

$$C = (1-\phi)C_\alpha + \phi C_\gamma \quad (4)$$

The redistribution of carbon between austenite and ferrite within the interface is approximated by [29]:

$$C_\alpha - C^*_\alpha = \frac{k_{\alpha\gamma}}{k_{\gamma\alpha}}(C_\gamma - C^*_\gamma) \quad (5)$$

where C^*_α and C^*_γ are the equilibrium carbon concentrations, $k_{\alpha\gamma}$ and $k_{\gamma\alpha}$ are the slopes of equilibrium carbon-concentration lines on a linearized phase diagram [29]. For the Fe–C–Mn system, the equilibrium carbon concentration is determined based on para-equilibrium.

2.2. Driving pressure for austenite–ferrite transformation

The chemical driving pressure for the ferrite-to-austenite transformation ($\alpha\to\gamma$) is described by:

$$\Delta G^t_{\alpha\to\gamma} = \chi_{\alpha\to\gamma}(C_\gamma - C^*_\gamma) \quad (6)$$

where $\chi_{\alpha\to\gamma}$ is a positive constant that is calculated with Thermo-calc® (TCFE7 database). The chemical driving pressure for the reverse austenite-to-ferrite transformation ($\gamma\to\alpha$) is given by $\Delta G^t_{\gamma\to\alpha} = -\Delta G^t_{\alpha\to\gamma}$.

For the Fe–C–Mn alloy, a part of the chemical driving pressure on an austenite/ferrite interface (Eq. (6)) is dissipated by the trans-interface diffusion of Mn, such that the driving pressure for interface migration in the phase-field equation (Eq. (1)) is:

$$\Delta G_{\alpha\to\gamma} = \Delta G^t_{\alpha\to\gamma} - \Delta G^{dis} \quad (7)$$

where the dissipated Gibbs-energy (ΔG^{dis}) is given by [24,30]:

$$\Delta G^{dis} = \int_{-\Lambda}^{+\Lambda}(x^0_{Mn} - x_{Mn}(y))\frac{dE(y)}{dy}dy \quad (8)$$

Here 2Λ is the physical interface thickness that is distinct from the numerical interface thickness η in the phase-field model, x^0_{Mn} is the molar fraction of Mn in the bulk, x_{Mn} is the molar fraction of Mn across the interface and $E(y)$ is the interaction potential of solute Mn with the austenite/ferrite interface. A wedge-shaped profile is assumed for the Mn-interface interaction potential [24], as shown in Fig. 1, where E_0 is the Mn-interface binding energy and $2\Delta E$ is the potential difference between ferrite and austenite which is calculated with Thermo-calc®. It is noted that the Mn-interface interaction potential will become a linear interpolation between the chemical potentials in ferrite and austenite, if the binding energy (E_0) is zero.

The concentration profile ($x_{Mn}(y)$) of the substitutional element (Mn) across an interface moving with a velocity of V is given by [24]:

$$D^{Mn}_{\text{int}}\frac{\partial x_{Mn}(y)}{\partial y} + \frac{D^{Mn}_{\text{int}}x_{Mn}(y)}{RT}\frac{\partial E(y)}{\partial y} + V(x_{Mn}(y) - x^0_{Mn}) = 0 \quad (9)$$

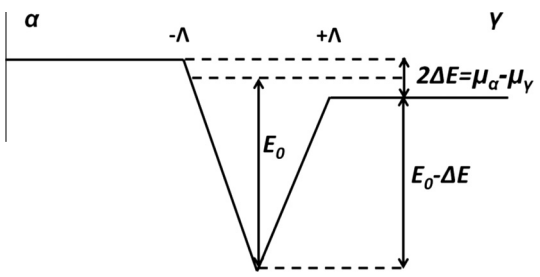

Fig. 1. Schematic of the chemical potential of Mn inside the austenite/ferrite interface with a nonzero binding energy (Λ is half of the interface; E_0 is binding energy; μ_α and μ_γ are chemical potentials of Mn in ferrite and austenite respectively).

where x^0_{Mn} is the molar fraction of Mn in the bulk and D^{Mn}_{int} is the diffusivity of solute Mn across the austenite/ferrite interface. An analytical solution of Eq. (9) was obtained by Purdy and Bréchet [24]. Further, a closed-form expression of the dissipated Gibbs-energy (Eq. (8)) is obtained:

$$\Delta G^{dis} = -\frac{RTx^0_{Mn}}{V_m}\left\{-\frac{a^2 v}{1+a}-\frac{b^2 v}{1+b}+\frac{a^2(1-\exp(-v(1+a)))}{(1+a)^2}+\frac{b^2(1-\exp(-v(1+b)))}{(1+b)^2}-\frac{ab(1-\exp(-v(1+a)))(1-\exp(-v(1+b)))}{(1+a)(1+b)}\right\} \quad (10)$$

where V_m is the molar volume of the matrix and

$$v = \frac{V\Lambda}{D^{Mn}_{\text{int}}}$$

$$a = \frac{1}{v}\cdot\frac{\Delta E - E_0}{RT}$$

$$b = \frac{1}{v}\cdot\frac{\Delta E + E_0}{RT}$$

Fig. 2 illustrates the dissipated Gibbs-energy for different values of the binding energy. Gibbs-energy dissipation occurs even if the binding energy of solute atoms to the interface is zero. Gibbs-energy dissipation also occurs at a stationary interface. Based on Eqs. (6) and (7), at a stationary interface where the effective driving pressure is zero, the carbon concentration is given by:

$$C_\gamma = C^*_\gamma + \frac{\Delta G^{dis}_0}{\chi_{\alpha\to\gamma}} \quad (11)$$

where ΔG^{dis}_0 is the dissipated Gibbs-energy on a stationary interface which does not depend on the binding energy. Eq. (11) indicates that the carbon concentration on a stationary interface is not the para-equilibrium concentration (C^*_γ) but is given by negligible-partitioning local equilibrium (NPLE) as proved by Odqvist et al. [31].

There are two possible conditions for an austenite/ferrite interface, i.e. $\Delta G^t_{\alpha\to\gamma} \geqslant 0$ in which case ferrite tends to transform to austenite and $\Delta G^t_{\alpha\to\gamma} \leqslant 0$ in which case austenite tends to transform to ferrite. A stationary interface can only start moving if the magnitude of the chemical driving pressure is greater than the dissipated Gibbs-energy, i.e. $|\Delta G^t_{\alpha\to\gamma}| > \Delta G^{dis}_0$. Otherwise the driving pressure ($\Delta G_{\alpha\to\gamma}$) is forced to zero and the interface remains stationary. This postulation will be used to mimic the stagnant stages in cyclic phase transformations.

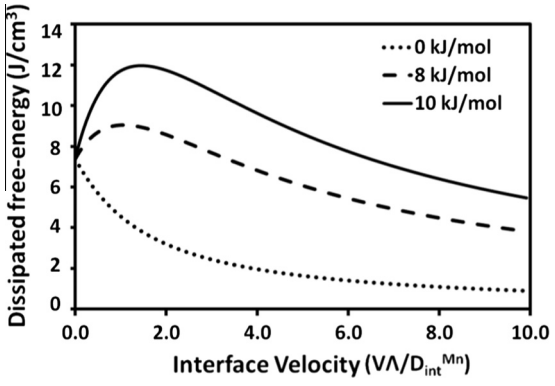

Fig. 2. Schematic of the dissipated Gibbs-energy for different values of the binding energy E_0.

A finite-difference method with an explicit Euler scheme is used to solve the phase-field and diffusion equations. A parallel C++ code using OpenMP and Message Passing Interfaces (MPI) is developed and implemented on computer clusters. The simulation domain is discretized with a Cartesian grid. The first and second derivatives in Eqs. (1) and (3) are approximated with five-point stencils. For a given grid point i at time t, the time derivative $\partial\phi/\partial t$ is approximated with $(\phi^t_i - \phi^{t-\Delta t}_i)/\Delta t$ where Δt is the time step, and the spatial derivative, e.g. $\partial\phi/\partial x$, is approximated with $(\phi^t_{i+1} - \phi^t_{i-1})/2\Delta x$ where Δx is the grid spacing. The interface velocity at each grid point (V) is calculated with $|\partial\phi/\partial t|/|\partial\phi/\partial n|$ where $\partial\phi/\partial n$ is the gradient of the phase field variable given by $(\partial\phi/\partial x, \partial\phi/\partial y)$ for 2D simulations. The driving pressure in the phase field equation is calculated with Eq. (7). The chemical driving pressure ($\Delta G^t_{\gamma\to\alpha}$), as a function of the carbon concentration, is evaluated at each grid point and averaged in the normal direction of an interface, because the potential variation of the chemical driving pressure in the normal direction of an interface can lead to numerical instability, e.g. interface spreading. Similarly, the dissipated Gibbs-energy ($\Delta G^{dis}(V)$), as a closed-form expression of the interface velocity (Eq. (10)), is evaluated with the average velocity in the normal direction of an interface.

3. Simulation conditions

Phase-field simulations have been conducted for cyclic phase transformations in the Fe–0.1 wt%C and Fe–0.1 wt%C–0.5 wt%Mn alloys, which were experimentally studied using dilatometry [11,32]. The Fe–C alloy without alloying elements is used as a benchmark case. Two different thermal paths, i.e. H-type and I-type, were considered for the cyclic phase transformations, as illustrated in Fig. 3. In both cases, the material was first fully austenitized at 1000 °C and then cooled down to T_a for 20 min isothermal holding to create a mixed ferrite–austenite microstructure. The temperature was then cycled between T_a and T_b with isothermal holding (H type) or without isothermal holding (I type) at T_a and T_b. The cycling temperatures as shown in Fig. 3, i.e. $[T_a, T_b]$, are located in the two-phase field (intercritical region) of the phase diagram, as listed in Table 1. Ferrite fractions are calculated based on the dilatation data using the lever-rule analysis assuming linear thermal expansion of ferrite and austenite. As shown in Fig. 4, the linear parts of the dilatation curves above 850 °C and below 750 °C are assumed to correspond to 100% austenite and ferrite respectively and they are linearly extrapolated to the two-phase region between 750 °C and 850 °C. For a given temperature, the ferrite fraction is given by the ratio BC/AC as shown in Fig. 4.

A region of $400 \times 400\ \mu m^2$ is selected from the micrographs that were obtained in the experimental studies before cyclic heat treatments (Figs. 5 and 6) [33] to provide the initial microstructure for each simulation. The intercritical austenite transforms to martensite during quenching and the ferritic and martensitic phases are distinguished by image contrast using MATLAB®. Neither ferrite nor austenite grain boundaries are resolved. The carbon concentration in ferrite is set to 0.001 wt% and the concentration in austenite is adjusted such that the average concentration is 0.1 wt%. Insulated (no-flux) boundary conditions are used, i.e. $\partial\phi/\partial n = 0$ and $\partial C/\partial n = 0$ at domain boundaries where n is the normal vector of a domain boundary, such that the total amount of carbon in the simulation domain is constant during a simulation. Based on the experimental observations no nucleation is assumed to take place during the cyclic phase transformations.

The ferrite/austenite interface energy is assumed to be $0.4\ J/m^2$ [6]. The activation energy of the ferrite/austenite interface mobility is taken to be 140 kJ/mol and the pre-factor is kept adjustable. The carbon diffusivities in ferrite and austenite (the pre-factor and

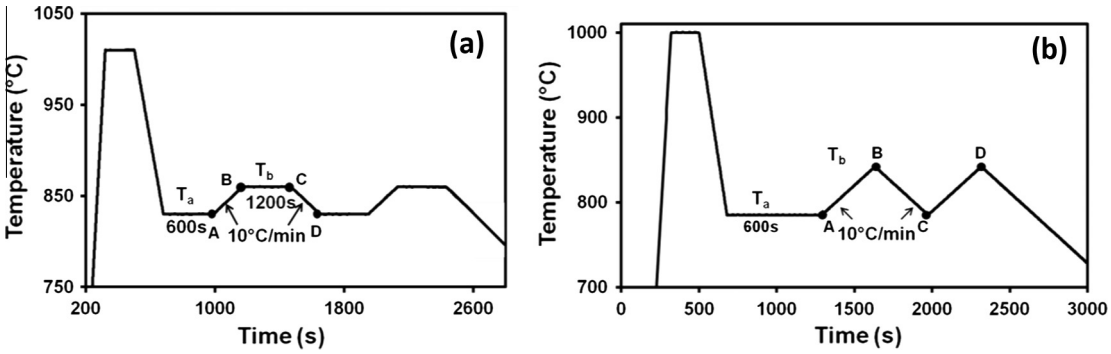

Fig. 3. Thermal paths for cyclic heat treatments: (a) H-type; (b) I-type.

Table 1
Maximum and minimum temperatures for cyclic heat treatments.

Steel chemistry	I-type		H-type	
	T_a	T_b	T_a	T_b
Fe–0.1 wt%C	815	855	830	860
Fe–0.1 wt%C–0.5 wt%Mn	785	842	780	835

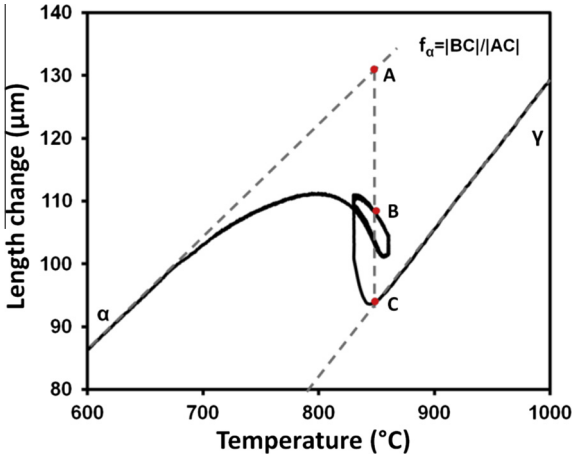

Fig. 4. Schematic of the lever-rule analysis of dilatation data.

activation energy) are listed in Table 2. The binding energy of Mn is taken to be 9.9 kJ/mol [34]. The physical interface thickness 2Λ is assumed to be 1 nm [2]. The trans-interface diffusivity of Mn is taken as the geometric average of the bulk diffusivities in ferrite and austenite [2,35], given by:

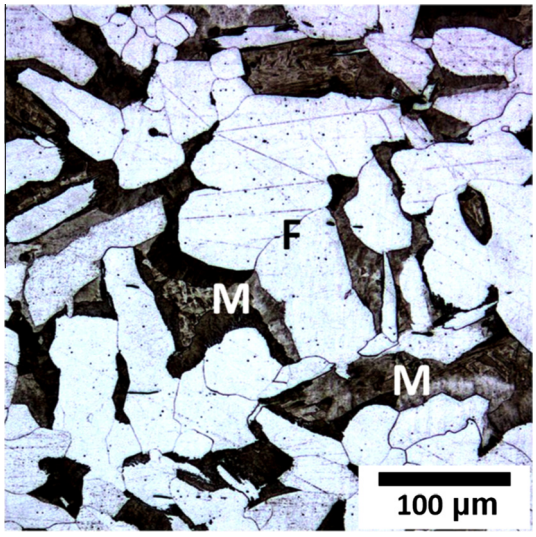

Fig. 6. Micrograph of the Fe–0.1 wt%C–0.5 wt%Mn alloy obtained by quenching from 780 °C (M: martensite; F: ferrite), used for both H-type and I-type simulations.

$$D_{\text{int}}^{M} = 0.5 \exp\left(-\frac{247650}{RT}\right) \text{cm}^2/\text{s} \tag{12}$$

A phase-field interface thickness η of $5\Delta x$ is used based on a previous sensitivity study [36,37]. A grid spacing Δx of 0.1 μm has been selected based on a sensitivity analysis such that a decrease of the grid spacing to 0.05 μm has a negligible influence on the transformation kinetics in the present simulations, i.e. the change of ferrite fractions is less than 0.05. To evaluate whether the selection of

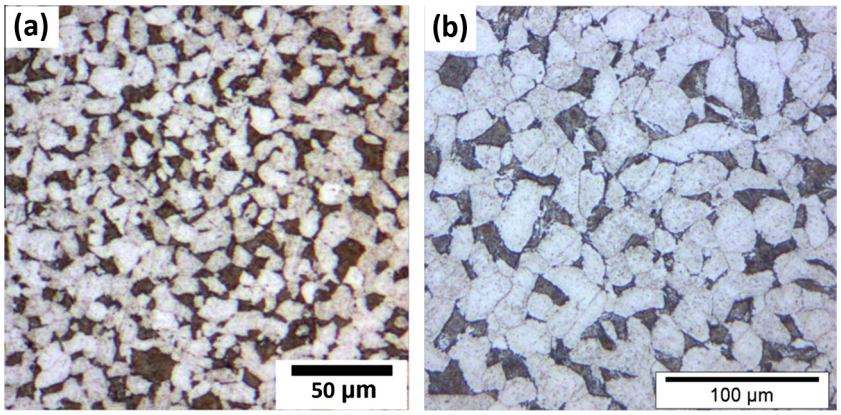

Fig. 5. Micrographs of the Fe–0.1 wt%C alloy obtained by quenching from 830 and 815 °C (light: ferrite; dark: martensite): (a) H-type; (b) I-type.

Table 2
Carbon diffusivities in ferrite and austenite [8].

Phase	Pre-factor (m^2/s)	Activation energy (kJ/mol)
C diffusivity in Ferrite	2.2×10^{-4}	125
C diffusivity in Austenite	0.15×10^{-4}	142

initial microstructures from the micrographs affects the transformation kinetics in the simulations, additional simulations with the initial microstructures selected from other micrographs were performed. It was found that at any temperature the difference between the simulated ferrite fractions obtained with different initial microstructures is less than 0.05, implying that the simulation results are statistically meaningful and not affected by the selection of initial microstructures.

4. Results and discussion

4.1. Fe–C alloy

Simulations of both the H-type and I-type cyclic heat treatments with two heating/cooling cycles were carried out for the Fe–C alloy. The mobility pre-factor ($m^0_{\alpha\gamma}$) is set to a sufficiently high value, i.e. 5×10^{-6} $m^4/(J\,s)$, such that any further increase has no effect on transformation rate, i.e. the phase transformation is diffusion-controlled. The simulated transformation kinetics is compared with the experimental results in Fig. 7. The equilibrium ferrite fraction as a function of temperature is also plotted as a reference.

First of all, it is found that during isothermal holding at 860 °C in the H-type heat treatment (Fig. 7(a)), the experimentally measured austenite fraction (0.83) is higher than the equilibrium fraction (0.78), which is contradictory to the fact that the formed austenite during ferrite to austenite transformation should not exceed the equilibrium fraction at any given temperature. Similarly, during heating from 815 °C to 855 °C for the I-type heat treatment, the experimentally measured austenite fraction is larger than the equilibrium fraction. Such discrepancies between the experimental data and the thermodynamic data may be related to the inaccuracy of either experimental measurements or the conversion of dilatation data to phase fractions using the lever rule. One of the experimental inaccuracies is the uncertainty of temperature measurements (±5 °C). It can be concluded from Fig. 7 that if the actual temperature in the specimens was higher than the measured value, the discrepancy between experimental data and thermodynamic equilibrium could be rationalized. For example, a temperature shift of 2 °C in the H-type case will lead to the experimentally measured fractions after holding at 860 °C equal to the thermodynamic equilibrium; a shift of 5 °C in the I-type case will bring the experimentally measured ferrite fractions into a reasonable relationship with respect to the thermodynamic equilibrium, i.e. ferrite fractions during austenite formation at the heating stage are larger than the equilibrium fractions. According to the equilibrium lines in Fig. 7, the equilibrium phase fractions are more sensitive to temperature at higher temperatures. For example, a temperature increase of 5 °C near 860 °C leads to a decrease of the equilibrium ferrite fraction by 0.1. Regardless of the inaccuracy of the experimental data, the simulated ferrite fractions agree well with the experimental data at lower temperatures, i.e. below 850 °C in the H-type case (Fig. 7(a)). But there are discrepancies at higher temperatures, as described above. In the I-type case (Fig. 7(b)), the simulated ferrite fractions are larger than the experimental data in the entire cycle. For example, the simulated ferrite fraction at 855 °C is 0.40 as compared to the experimental measurement of 0.24.

Taking the inaccuracy of temperature measurements into account, simulations with an increase of the overall temperatures by 2 °C and 5 °C were carried out for the H-type and I-type cases, respectively. The temperature range [T_a, T_b] is changed to [832 °C, 862 °C] for the H-type case and [820 °C, 860 °C] for the I-type case. As shown in Fig. 8, the simulated transformation kinetics is in much better agreement with the experimental data in both cases. The simulation results indicate that the assumption of a carbon diffusion-controlled phase transformation is appropriate. The ferrite fraction keeps changing during both heating and cooling in the H-type case, i.e. no stagnant stage. In the I-type case, upon cooling from 855 °C, austenite does not transform back to ferrite immediately. Instead, ferrite to austenite transformation continues until cooling to 853 °C. The austenite formation during cooling is due to the non-equilibrium condition in the material upon cooling such that there is still a driving pressure for austenite formation. Below 853 °C, the inverse process, i.e. the austenite-to-ferrite transformation, takes place. Although the ferrite fractions at temperatures between 850 °C and 855 °C change insignificantly, it is not a stagnant stage. In fact, the ferrite/austenite interfaces keep moving in this temperature range and reverse directions at 853 °C. Based on the present model, there is no Gibbs-energy dissipation in the plain-carbon steel. Thus the driving pressure for interface migration ($\Delta G_{\alpha\to\gamma}$) does not remain zero for any temperature range during the cooling stage. The heating stage has a similar situation. Therefore, there is no stagnant stage in either the H-type or the I-type case for the Fe–C alloy.

The simulated microstructures at selected stages of the H-type heat treatment are shown in Fig. 9. The back-and-forth motion of α/γ interfaces has been described in the phase-field simulation. At the heating stage, the isolated austenite grains grow into ferrite and some of them impinge with each other. At the cooling stage, the α/γ interfaces move in the reverse direction and austenite transforms back to ferrite.

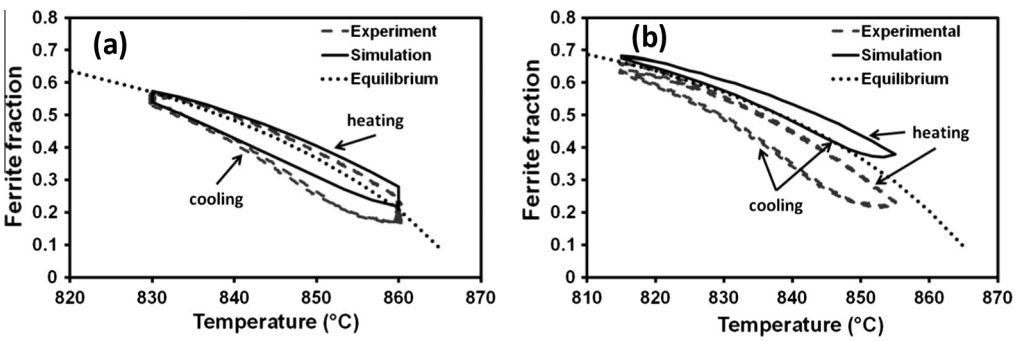

Fig. 7. Comparison of simulated transformation kinetics and thermodynamically equilibrium ferrite fractions with experimental data for Fe–0.1 wt%C: (a) H-type; (b) I-type.

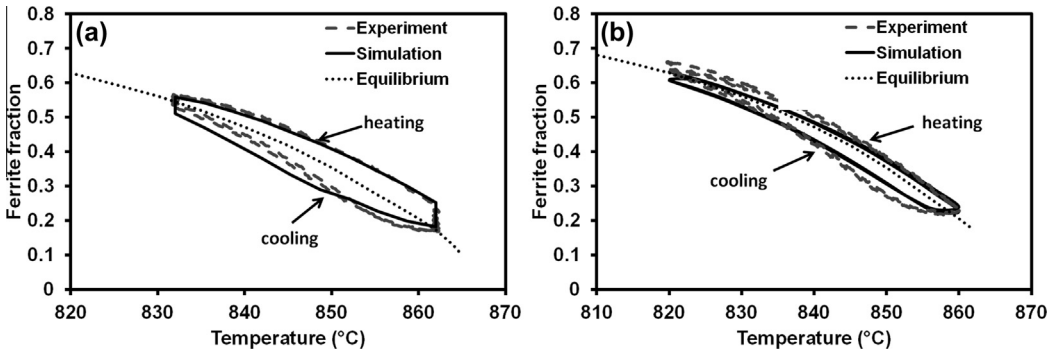

Fig. 8. Comparison of simulated transformation kinetics and thermodynamically equilibrium ferrite fractions with experimental data for Fe–0.1 wt%C with a temperature shift of 2 °C in H-type case (a) and 5 °C in the I-type (b).

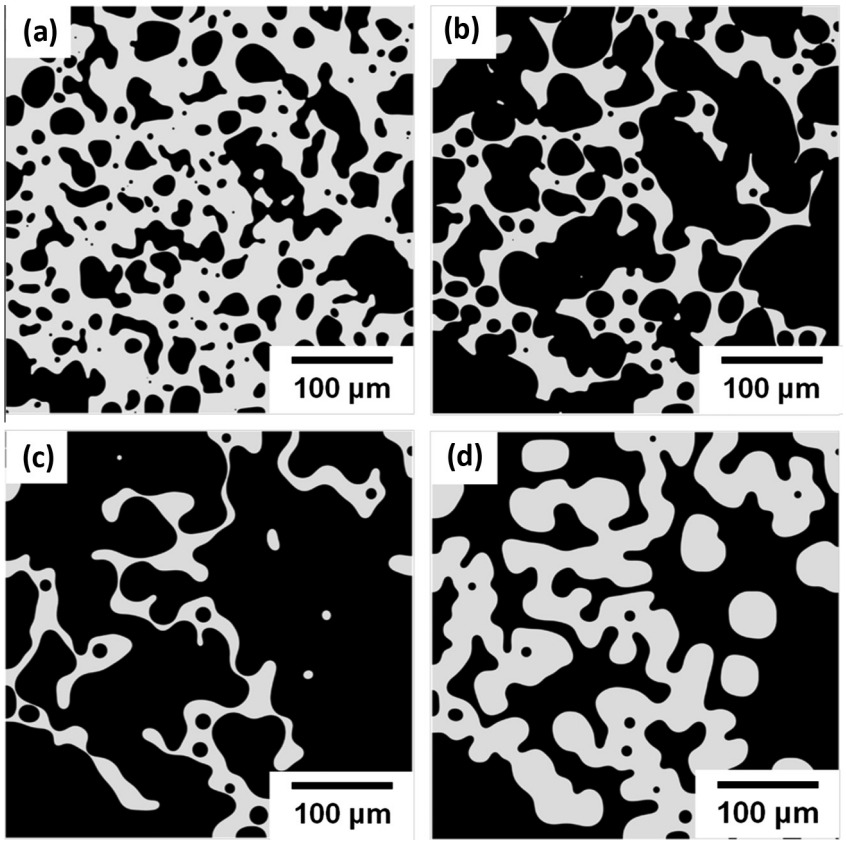

Fig. 9. Simulated microstructures (dark: austenite; light: ferrite) at selected stages of the H-type heat treatment (+5 °C) for Fe–0.1 wt%C, corresponding to each marked point (A–D) on the thermal-history curves shown in Fig. 3(a)).

4.2. Fe–C–Mn alloy

Four simulations were carried out, i.e. for two types of thermal paths each with and without a temperature shift of 5 °C, i.e. the upper bound of the uncertainty of temperature measurements in the experiments. The value of 5×10^{-6} m^4/(J s) for the pre-factor of the α/γ interface mobility that is employed for the Fe–C alloy is used in the simulations for the Fe–C–Mn alloy. It is found that any increase of the interface mobility has a negligible influence on the transformation kinetics, whereas an decrease below 1×10^{-6} m^4/(J s) leads to slower transformation rates.

There are various equilibria in the ternary Fe–C–Mn system, e.g. para-equilibrium, ortho-equilibrium and negligible-partitioning local equilibrium (NPLE). For a given temperature, NPLE is defined by a specific tie-line where the Mn concentration in the product phase is equal to the concentration of the bulk x^0_{Mn} (Fig. 10) [14,38]. Therefore, the NPLE tie-line depends on the direction of the austenite–ferrite transformation, i.e. either the austenite-to-ferrite transformation ($\gamma \rightarrow \alpha$) or the ferrite-to-austenite transformation ($\alpha \rightarrow \gamma$). For $\gamma \rightarrow \alpha$, the product phase is ferrite and thus the relevant NPLE tie-line connects ferrite with a concentration of x^0_{Mn} [14]. On the other hand, for $\alpha \rightarrow \gamma$, the product phase is austenite and thus the relevant NPLE tie-line connects austenite with a concentration of x^0_{Mn} (Fig. 10) [38].

The simulated transformation kinetics is compared with the experimental data for the I-type thermal path in Fig. 11. NPLE is selected to calculate the equilibrium ferrite fraction used as a reference, because the present phase-field model mimics NPLE at a

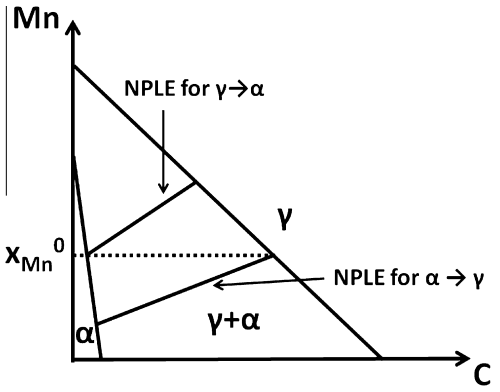

Fig. 10. Illustration of NPLE tie-lines non an isothermal section of a Fe–C–Mn ternary phase diagram.

stationary interface. The initial microstructure used in the simulation is formed during the austenite-to-ferrite transformation ($\gamma \rightarrow \alpha$) at 785 °C (Fig. 3(b)). The agreement of the experimentally measured ferrite fraction with the ferrite fraction of NPLE for $\gamma \rightarrow \alpha$ implies that the austenite-to-ferrite transformation ($\gamma \rightarrow \alpha$) has reached NPLE. But after a full heating/cooling cycle, the ferrite fraction at 785 °C is smaller than the fraction of NPLE for $\gamma \rightarrow \alpha$ in both experiments and simulations, indicating a non-equilibrium condition, i.e. the austenite-to-ferrite transformation ($\gamma \rightarrow \alpha$) is incomplete in terms of NPLE.

In the case without a temperature shift, the simulated transformation kinetics is not in agreement with the experimental data at the highest temperature (Fig. 11(a)). The ferrite fraction at 840 °C is 0.08 above the experimental measurement. On the other hand, the simulation results are in better agreement with experimental data in the case with the temperature increase of 5 °C (Fig. 11(b)). In particular, the phase fractions at both the lowest and highest temperatures are consistent with the experimental data.

Distinct from the Fe–C alloy, there is a stagnant stage for the ferrite-to-austenite transformation during heating and for the austenite-to-ferrite transformation during cooling, respectively. As shown in the case with the temperature shift (Fig. 11(b)), the experimental ferrite fraction does not decrease significantly upon heating until about 810 °C, implying a sluggish transition of ferrite to austenite; the ferrite fraction does not increase significantly upon cooling until about 830 °C, implying a sluggish transition of austenite to ferrite. These stagnant stages have been quantitatively replicated in the phase-field simulation, with a temperature-range width of about 20 °C. The good description of transformation kinetics by the phase-field model indicates that the assumption of carbon diffusion only is reasonable and long-range diffusion of Mn is insignificant during the I-type heat treatment. Fig. 12 shows the microstructures at selected stages of I-type cycles. The microstructure after a heating/cooling cycle generally resembles the one before the cycle.

The simulated transformation kinetics for the H-type heat treatment is compared with the experimental data in Fig. 13. The austenite-to-ferrite transformation ($\gamma \rightarrow \alpha$) takes place during cooling and holding at 780 °C, whereas the ferrite-to-austenite transformation ($\alpha \rightarrow \gamma$) takes place during heating and holding at 835 °C. The phase-field model generally describes also the trend of cyclic phase transformations for the H-type heat treatment of the Fe–C–Mn alloy. In particular, the stagnant stages for both heating and cooling are replicated quantitatively by the model, with a temperature-range width of about 20 °C. The simulated ferrite fractions are consistent with the experimental data at low temperatures, e.g. below 810 °C. Both the simulated and the experimentally measured ferrite fractions at 780 °C are consistent with the ferrite fraction of NPLE for $\gamma \rightarrow \alpha$, implying that the austenite-to-ferrite transformation ($\gamma \rightarrow \alpha$) induced by long-range diffusion of Mn is negligible. According to the local-equilibrium theory by Coates [14], the austenite-to-ferrite transformation ($\gamma \rightarrow \alpha$) is carbon diffusion-controlled first (NPLE) and Mn diffusion-controlled subsequently (partitioning local equilibrium, PLE). If long-range diffusion of Mn occurs, the migration distance of a ferrite/austenite interface can be approximated with the Mn diffusion distance in the parent phase, i.e. austenite. In the present case, holding at 780 °C for 600 s leads to a diffusion length of about 14 nm (the diffusivity of Mn in austenite is about 1.7×10^{-6} μm²/s at 780 °C [35]) that is negligible in comparison with an average ferrite grain size of 10–15 μm. Thus, long-range diffusion of Mn is negligible and the assumption of carbon diffusion only is appropriate for the austenite-to-ferrite transformation ($\gamma \rightarrow \alpha$).

The experimentally measured ferrite fraction at 835 °C (0.2–0.25) in the H-type case is, however, smaller than the ferrite fraction in the simulation which is equal to the ferrite fraction of NPLE for $\alpha \rightarrow \gamma$ (0.35), or rather the fraction of formed austenite is larger than the NPLE austenite fraction, implying that long-range diffusion of Mn occurs and induces further austenite formation. Based on the local-equilibrium model by Wycliffe et al. [38], the ferrite-to-austenite transformation ($\alpha \rightarrow \gamma$) is carbon diffusion-controlled first (NPLE) and Mn diffusion-controlled subsequently (partitioning local equilibrium, PLE). If long-range diffusion of Mn occurs, the migration distance of a ferrite/austenite interface can be approximated with the Mn diffusion distance in the parent phase, i.e. ferrite. In the present case, holding at 835 °C for 1200 s leads to a diffusion length of about 1.3 μm (the diffusivity of Mn in ferrite is about 1.5×10^{-3} μm²/s at 835 °C [35]). An increase of 1.3 μm in the equivalent radius of austenite grains with an average size of 40–50 μm will contribute to a volume fraction 0.12–0.16 if a spherical shape is assumed in the present case, which is consistent

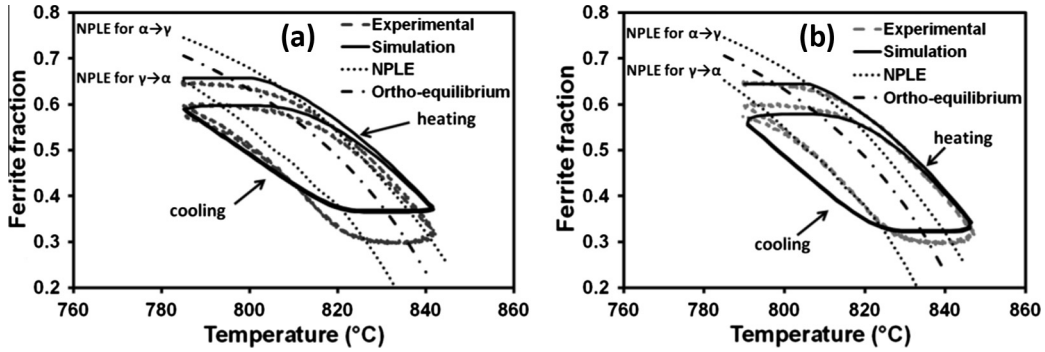

Fig. 11. Comparison of simulated transformation kinetics and NPLE ferrite fractions with experimental data (I-type) for Fe–0.1 wt%C–0.5 wt%Mn: (a) unshifted temperature; (b) shifted temperature (+5 °C).

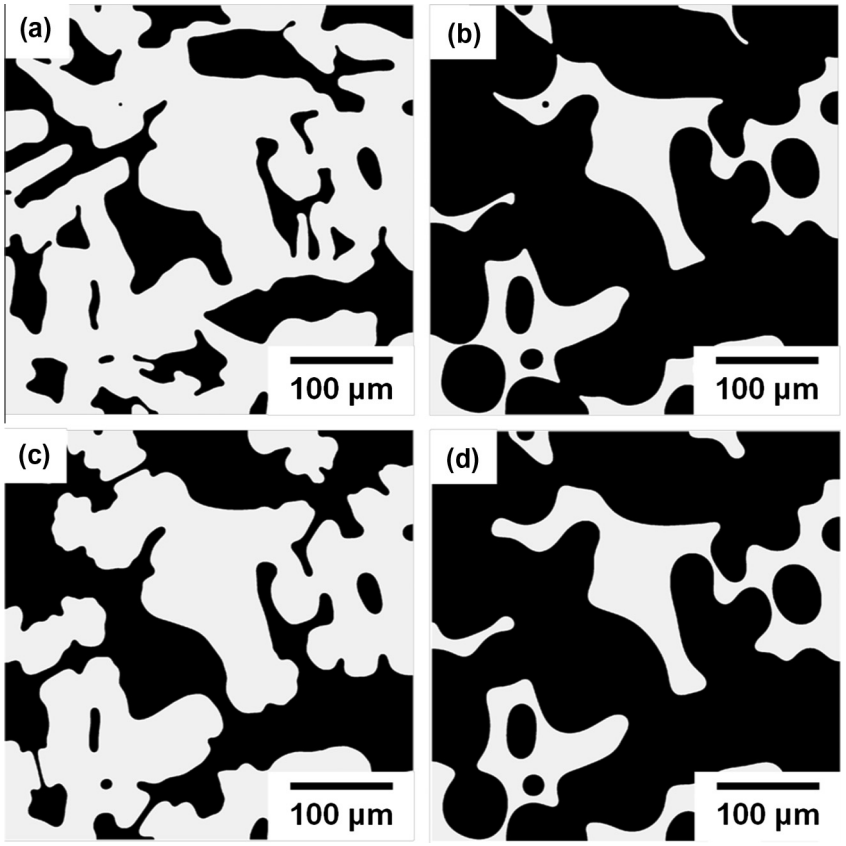

Fig. 12. Simulated microstructures (dark: austenite; light: ferrite) at selected stages of the I-type heat treatment for Fe–0.1 wt%C–0.5 wt%Mn, corresponding to each marked point (A–D) on the thermal-history curve shown in Fig. 3(b)).

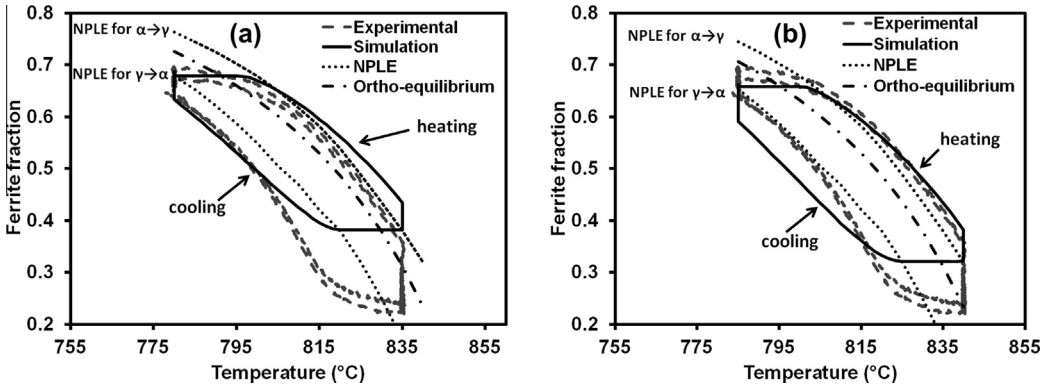

Fig. 13. Comparison of simulated transformation kinetics and NPLE ferrite fractions with experimental data (H-type) for Fe–0.1 wt%C–0.5 wt%Mn: (a) unmodified temperature; (b) modified temperature (+5 °C).

with the difference between the simulated and the experimentally measured austenite fractions at 835 °C.

Therefore, the present phase-field model considering carbon diffusion only is applicable to the I-type thermal path, but not applicable to the H-type thermal path where long-time holding at the upper temperature T_b leads to significant long-range diffusion of Mn during the ferrite-to-austenite transformation.

5. Conclusions

In this work, a 2D phase-field model, which considers the energy dissipation due to Mn diffusion inside the interface, has been used to describe cyclic phase transformations in the Fe–0.1 wt%C and Fe–0.1 wt%C–0.5 wt%Mn alloys. The phase-field model predicts that there is no stagnant stage in the Fe–C alloy, while stagnant stages exist in the Fe–C–Mn alloy. The occurrence of the stagnant stages is rationalized with Gibbs-energy dissipation induced by trans-interface diffusion of Mn. Accounting for this role of Mn enables to replicate the cyclic transformation kinetics without the previously proposed introduction of an effective mobility that is different for the austenite and ferrite formation stages. The model proposed here remains valid as long as there is no substantial bulk diffusion of Mn, e.g. for the I-type thermal cycles, whereas for the longer holding times at higher temperatures in the H-type cycles long-range redistribution of Mn (and other substitutional solutes) is significant.

Acknowledgement

The authors are grateful to the Natural Sciences and Engineering Research Council of Canada (NSERC) for financial support.

References

[1] M. Kulakov, W.J. Poole, M. Militzer, Metall. Mater. Trans. A 44 (2013) 1–13, http://dx.doi.org/10.1007/s11661-013-1721-z.
[2] T. Jia, M. Militzer, ISIJ Int. 52 (2012) 644–649. http://dx.doi.org/10.2355/isijinternational.52.644.
[3] H.S. Zurob, C.R. Hutchinson, Y. Bréchet, H. Seyedrezai, G.R. Purdy, Acta Mater. 57 (2009) 2781–2792, http://dx.doi.org/10.1016/j.actamat.2009.02.029.
[4] H.S. Zurob, D. Panahi, C.R. Hutchinson, Y. Bréchet, G.R. Purdy, Metall. Mater. Trans. A 44 (2013) 3456–3471, http://dx.doi.org/10.1007/s11661-012-1479-8.
[5] H. Guo, M. Enomoto, Metall. Mater. Trans. A 38 (2007) 1152–1161, http://dx.doi.org/10.1007/s11661-007-9139-0.
[6] M. Militzer, Curr. Opin. Solid State Mater. Sci. 15 (2011) 106–115, http://dx.doi.org/10.1016/j.cossms.2010.10.001.
[7] C.-J. Huang, D.J. Browne, Metall. Mater. Trans. A 37 (2006) 589–598, http://dx.doi.org/10.1007/s11661-006-0031-0.
[8] M. Militzer, M.G. Mecozzi, J. Sietsma, S. van der Zwaag, Acta Mater. 54 (2006) 3961–3972, http://dx.doi.org/10.1016/j.actamat.2006.04.029.
[9] M.G. Mecozzi, J. Sietsma, S. van der Zwaag, Acta Mater. 54 (2006) 1431–1440, http://dx.doi.org/10.1016/j.actamat.2005.11.014.
[10] C. Zheng, D. Raabe, D. Li, Acta Mater. 60 (2012) 4768–4779, http://dx.doi.org/10.1016/j.actamat.2012.06.007.
[11] H. Chen, S. van der Zwaag, Acta Mater. 61 (2013) 1338–1349, http://dx.doi.org/10.1016/j.actamat.2012.11.011.
[12] H. Chen, B. Appolaire, S. van der Zwaag, Acta Mater. 59 (2011) 6751–6760, http://dx.doi.org/10.1016/j.actamat.2011.07.033.
[13] J.S. Kirkaldy, Can. J. Phys. 36 (1958) 907–916, http://dx.doi.org/10.1139/p58-097.
[14] D.E. Coates, Metall. Trans. 4 (1972) 1973–2313, http://dx.doi.org/10.1007/BF02669370.
[15] C.J. Zener, Appl. Phys. 20 (1949) 950–957.
[16] M. Hillert, Introduction to Paraequilibrium, Internal Report of the Swedish Institute for Metal Research, 1953.
[17] A. Hultgren, Trans. ASM 39 (1947) 915–922.
[18] E. Gamsjäger, H. Chen, S. van der Zwaag, Comput. Mater. Sci. 83 (2014) 92–100, http://dx.doi.org/10.1016/j.commatsci.2013.10.036.
[19] C.J. Huang, D.J. Browne, S. McFadden, Acta Mater. 54 (2006) 11–21, http://dx.doi.org/10.1016/j.actamat.2005.08.033.
[20] M.G. Mecozzi, J. Sietsma, S. Van Der Zwaag, M. Apel, P. Schaffnit, I. Steinbach, Metall. Mater. Trans. A 36 (2005) 2327–2340, http://dx.doi.org/10.1007/s11661-005-0105-4.
[21] M.G. Mecozzi, M. Militzer, J. Sietsma, S. van der Zwaag, Metall. Mater. Trans. A 39 (2008) 1237–1247, http://dx.doi.org/10.1007/s11661-008-9517-2.
[22] H. Chen, S. Van Der Zwaag, Acta Mater. 72 (2014) 1–12, http://dx.doi.org/10.1016/j.actamat.2014.03.034.
[23] J.W. Cahn, Acta Metall. 10 (1962) 789–798, http://dx.doi.org/10.1016/0001-6160(62)90092-5.
[24] G.R. Purdy, Y.J.M. Bréchet, Acta Metall. Mater. 43 (1995) 3763–3774, http://dx.doi.org/10.1016/0956-7151(95)90160-4.
[25] M. Hillert, B. Sundman, Acta Metall. 24 (1976) 731–743, http://dx.doi.org/10.1016/0001-6160(76)90108-5.
[26] M. Hillert, J. Odqvist, J. Ågren, Scr. Mater. 45 (2001) 221–227, http://dx.doi.org/10.1016/S1359-6462(01)01022-3.
[27] I. Steinbach, F. Pezzolla, Phys. Nonlinear Phenom. 134 (1999) 385–393, http://dx.doi.org/10.1016/S0167-2789(99)00129-3.
[28] J. Sietsma, S. van der Zwaag, Acta Mater. 52 (2004) 4143–4152, http://dx.doi.org/10.1016/j.actamat.2004.05.027.
[29] J. Eiken, B. Böttger, I. Steinbach, Phys. Rev. E 73 (2006) 066122, http://dx.doi.org/10.1103/PhysRevE.73.066122.
[30] M. Hillert, Acta Mater. 47 (1999) 4481–4505, http://dx.doi.org/10.1016/S1359-6454(99)00336-5.
[31] J. Odqvist, M. Hillert, J. Ågren, Acta Mater. 50 (2002) 3213–3227, http://dx.doi.org/10.1016/S1359-6454(02)00143-X.
[32] H. Chen, R. Kuziak, S. van der Zwaag, Metall. Mater. Trans. A 44 (2013) 5617–5621, http://dx.doi.org/10.1007/s11661-013-2040-0.
[33] H. Chen, Cyclic Partial Phase Transformations In Low Alloyed Steels: Modeling and Experiments, Ph.D. Thesis. Delft University of Technology, Delft, Netherland, 2013.
[34] H. Chen, K. Zhu, L. Zhao, S. van der Zwaag, Acta Mater. 61 (2013) 5458–5468, http://dx.doi.org/10.1016/j.actamat.2013.05.034.
[35] S. Sun, M. Pugh, Mater. Sci. Eng. A 276 (2000) 167–174, http://dx.doi.org/10.1016/S0921-5093(99)00261-0.
[36] B. Zhu, M. Militzer, Model. Simul. Mater. Sci. Eng. 20 (2012) 08501, http://dx.doi.org/10.1088/0965-0393/20/8/085011.
[37] B. Zhu, M. Militzer, Metall. Mater. Trans. A 46 (2015) 1073–1084.
[38] P.A. Wycliffe, G.R. Purdy, J.D. Embury, Can. Metall. Q. 20 (1981) 339–350, http://dx.doi.org/10.1179/000844381795270174.